

Co-infiltration of nickel and mixed conducting $Gd_{0.1}Ce_{0.9}O_{2-\delta}$ and $La_{0.6}Sr_{0.3}Ni_{0.15}Cr_{0.85}O_{3-\delta}$ phases in Ni-YSZ anodes for improved stability and performance

Yanchen Lu^a, Paul Gasper^a, Alexey Nikiforov^b, Uday B. Pal^{a,c}, Srikanth Gopalan^{a,c}, and Soumendran Basu^{a,c,*}

^a Boston University Division of Materials Science and Engineering, Brookline, MA 02446, USA

^b Boston University Photonics Center, Boston, MA 02215, USA

^c Boston University Department of Mechanical Engineering, Boston, MA 02215, USA

* Corresponding author. Boston University Division of Materials Science and Engineering, Brookline, MA 02446, USA. Email address: basu@bu.edu

ABSTRACT

Liquid phase infiltration of nickel (Ni) nanoparticles in Ni/yttria-stabilized-zirconia (YSZ) cermet anodes for solid oxide fuel cells can improve anode performance provided that the infiltrated nanoparticles on YSZ connect to form conducting pathways and the Ni nanoparticles do not coarsen significantly. This study explores liquid phase co-infiltration of Ni with mixed conducting oxides, the latter providing microstructural stability and conductive pathways between Ni nanoparticles. Two mixed conducting oxides have been studied; $Gd_{0.1}Ce_{0.9}O_{2-\delta}$ (GDC), a predominantly ionic conductor, and $La_{0.6}Sr_{0.3}Ni_{0.15}Cr_{0.85}O_{3-\delta}$ (LSNC), a predominantly electronic conductor. Experimental results show that both oxides improve nickel nanoparticle stability and improve charge transfer kinetics. However, the electrochemical performance of the Ni-GDC infiltrated electrode is much better than that of the Ni-LSNC infiltrated electrode. This is attributed to the citrate-nitrate combustion reaction required to form LSNC, which fills the pores of the anode and inhibits gas diffusion, reducing the performance of the Ni-LSNC infiltrated electrode.

1. INTRODUCTION

Solid oxide fuel cells (SOFCs) are highly efficient energy conversion devices for generating electrical energy directly from stored chemical energy, with many potential applications both for traditional energy systems as well as renewable energy grids [1-3]. However, high operating temperatures of SOFCs, which can be over 800°C, limit their lifetimes and increase their cost. One of the critical issues for commercializing SOFCs is their high operating temperatures, which can be over 800°C. High temperatures are required for good cell performance, but result in higher material costs and long-term performance degradation compared to cells operated at lower temperatures of 700°C and below [4,5]. Therefore, substantial research efforts have directed at lower the operating temperature of SOFCs. However, operating cells at lower temperatures reduces cell performance due to slow electrode reaction kinetics. There are several approaches for improving electrode reaction kinetics at low temperatures; most focus on development of new materials or new electrode designs [6-9]. In particular, the development of electrodes with nanoscale features has been pursued to improve the kinetics of charge transfer reactions. These efforts have been buoyed by continued research into liquid infiltration as a manufacturing method for SOFC electrodes [10-12]. This is because liquid infiltration enables the formation of nanostructured phases *in-situ* at temperatures as low as 500°C. Such features cannot be incorporated during cell processing, since sintering requires temperatures in excess of 1300°C, which would lead to significant coarsening of any nanoscale microstructure.

Despite these efforts, the design of state-of-the-art SOFC anodes has not changed substantially in many years. The bulk of a standard SOFC anode consists of a several hundred micron thick porous nickel yttria-stabilized-zirconia (Ni-YSZ) cermet that provides mechanical support for the rest of the cell. A more finely structured porous Ni-YSZ layer, between 5 and 20 microns thick, is located between the anode support and the dense YSZ electrolyte. This finely structured layer, referred hereon as the anode active layer (AAL), is usually made up of sintered powders that are about one micron in diameter. By using liquid infiltration to introduce nickel particles with diameters of 100 nm or less into the AAL, the size of nickel features within the electrode can be reduced. This increases the density of triple phase boundaries (TPBs) that are the

intersections of the Ni, YSZ and pore phases, where the electrons, oxygen ions and the fuel all meet and react. The introduction of the Ni nanoparticles increases the TPB density, which has been shown to improve cell performance, especially at lower operating temperatures [13]. However, these infiltrated nickel nanostructures suffer from coarsening after just a few hours of operation [14-17]. In addition, the infiltrated nickel deposits as roughly hemispherical nanoparticles only on the YSZ grains. If these nanoparticles are isolated from one another, they are not electrically connected to the Ni-YSZ cermet, unless the Ni nanoparticle is directly located on a Ni-YSZ cermet TPB. As a result, most of the additional TPBs remain inert to (or unable to participate in) electrochemical reactions, and thus the advantages of liquid infiltration are not fully utilized [10,13,18]. In order to address the issues of Ni nanoparticle coarsening and formation of non-active TPBs, this research investigates the simultaneous infiltration of nickel with a mixed ionic-electronic conductor (MIEC). The introduction of an MIEC material into nickel infiltrated Ni-YSZ cermet anodes should both physically constrain the infiltrated nickel nanoparticles to prevent coarsening as well as electrochemically connect some or all of the Ni nanoparticles to the Ni-YSZ cermet, thereby improving cell performance and stability of infiltrated nickel nanoparticles.

Two groups of MIEC materials that are used often in SOFC anodes due to their high conductivity and chemical stability in the anode-operating environment are fluorites and perovskites [19]. Of these two groups, fluorites have high ionic conductivity, while perovskites have high electronic conductivity [6]. Gadolinium doped ceria ($\text{Gd}_{0.1}\text{Ce}_{0.9}\text{O}_{2-\delta}$) (GDC) is a good fluorite candidate for infiltration because it has higher ionic conductivity than YSZ as well as reasonable electronic conductivity at low oxygen partial pressures [20]. Also, a liquid solution of Gd and Ce nitrate salts can be easily infiltrated into Ni-YSZ anodes, and the nitrates can then be decomposed at around 500°C to form GDC nanostructures. Infiltrated GDC nanostructures have been utilized by several researchers and show consistent performance improvement compared to YSZ or traditionally sintered electrodes [21,22]. The improvement in cell performance after infiltration of GDC is attributed to the increased ionic conductivity of GDC compared to YSZ, which enables oxygen ions to travel farther away from the electrolyte, increasing the number of electrochemical

reaction sites and improving anodic charge transfer [22,23]. Simultaneous infiltration of GDC with metallic nanoparticles has been less studied. Skafte et al. infiltrated GDC into Ni-YSZ cermet anodes, showing improvement in initial cell performance after both GDC infiltration as well as simultaneous infiltration of GDC and copper nanoparticles [24]. The addition of copper substantially increased cell performance over the cell with only GDC, suggesting simultaneous infiltration of metallic nanoparticles with an MIEC can greatly improve the charge transfer kinetics of Ni-YSZ cermet anodes [24].

The infiltration of conducting perovskite oxides into Ni-YSZ cermet anodes has not received much research interest. Because of their high electrical conductivity, perovskite oxides have mainly been studied for the development of fully ceramic fuel cell anodes [6,8,25]. For selecting a perovskite composition that is suitable for infiltration into Ni-YSZ anodes, the first consideration is the chemical stability of the material in the anode operating environment, which sees oxygen partial pressures as low as 10^{-17} Pa at 800°C. Many cobaltite, ferrite, manganite, and nickelate perovskites become unstable at oxygen partial pressures lower than 10^{-2} Pa, 10^{-12} Pa, 10^{-10} Pa, and 10 Pa at 800°C, respectively [9]. However, many chromite, titanate, and vanadate perovskites are suitable for use in SOFC anodes. A chromite perovskite is the most suitable candidate for liquid infiltration because the nitrate precursors of titanium and vanadium are not readily available. For this study, A-site deficient Ni-doped lanthanum strontium chromite ($\text{La}_{0.6}\text{Sr}_{0.3}\text{Ni}_{0.15}\text{Cr}_{0.85}\text{O}_{3-\delta}$) (LSNC) is chosen. LSNC has high electrical conductivity in the anode-operating environment, and has been previously utilized as a material for an all-ceramic anode, exhibiting good electrochemical performance [26]. LSNC cannot be synthesized using the nitrate decomposition process, and the nitrate solution has to be mixed with citric acid to carry out the citric-nitrate auto combustion process as described in the next section.

In this work, cells with Ni-YSZ cermet anodes are co-infiltrated with Ni-GDC and Ni-LSNC to study their performance and the stability of the Ni-MIEC nanostructures. The GDC and LSNC phases are utilized both for physically stabilizing the infiltrated nickel nanoparticles as well as electrochemically connecting them to the Ni-YSZ substrate. GDC and LSNC have been chosen for their suitability for use in SOFC anodes

and to compare the impact of ionic and electronic conductivity of the MIEC phase (primarily ionic for GDC versus primarily electronic for LSNC) and processing technique (nitrate decomposition for GDC versus citric-nitrate auto combustion for LSNC) on cell performance. This study first validates the chemical stability of each material for use in the anode operating environment, then studies the physical stability of the infiltrated microstructures by exposing infiltrated anodes to 2% H₂ – 98% Ar and 25% H₂ – 75% H₂O gas mixtures at 800°C for 48 hours. The electrochemical performance of Ni-GDC and Ni-LSNC infiltrated Ni-YSZ anodes are evaluated using current-voltage (I-V) scans and electrochemical impedance spectroscopy (EIS). Performance measurements are analyzed to determine the relative contributions of the Ni-GDC and Ni-LSNC infiltration to the mass transfer and charge transfer resistances of the electrode. Comparison of the electrode microstructures after testing is used to examine the stability of the infiltrated phases after exposure to electrochemical current.

2. MATERIALS AND METHODS

2.1. Preparation of infiltration solutions and powder characterization

Ni, Ni-GDC and Ni-LSNC liquid infiltration solutions were synthesized using nickel nitrate (Ni(NO₃)₂·6H₂O, Chemsavers, USA), gadolinium nitrate (Gd(NO₃)₃·6H₂O, Alfa Aesar, USA), cerium nitrate (Ce(NO₃)₃·6H₂O, Alfa Aesar, USA), lanthanum nitrate (La(NO₃)₂·6H₂O, Sigma-Aldrich, USA), strontium nitrate (Sr(NO₃)₂, Sigma-Aldrich, USA), chromium nitrate (Cr(NO₃)₃·9H₂O, Alfa Aesar, USA), and citric acid (C₆H₈O₇, Alfa Aesar, USA). For each solution, stoichiometric amounts of metal nitrates and citric acid were dissolved in ethanol on a hot plate at 70°C while stirring. The compositions of precursor solutions used are listed in Table I.

To ensure proper formation of the MIEC phases, the liquid infiltration solutions were used to form powders in a container. The phase purity of the MIEC powders can be easily verified by x-ray diffraction (XRD) measurements. The powders were formed under the same environmental conditions the precursors would encounter for nanoparticle formation in infiltrated cells. Ni-MIEC powders were formed by heating the

liquid precursor in air to 320°C. This allows for the formation of Gd₂O₃, CeO₂, and NiO by the nitrate decomposition process (for Ni-GDC), and LSNC and NiO by the citric-nitrate auto-combustion process (for Ni-LSNC) [23,27,28]. Heating to 800°C while flowing a 2% H₂ – 98% Ar gas mixture at 300 cm³ min⁻¹ and holding at temperature for 8 hours ensures that the GDC phase is formed (Ni-GDC), and that NiO is reduced to Ni (both cases). The phases of the synthesized powders were then characterized by XRD using a D8 DISCOVER X-ray diffractometer (Bruker, USA) with Cu K- α radiation and analyzing the resulting spectra using DIFFRAC.EVA software (Bruker, USA).

Table I. Details of precursor solutions used in liquid infiltration

Infiltrant	Formula	Ni to MIEC molar ratio	Synthesis method	Citric acid to MIEC metal cations molar ratio	Metal solution molarity	Rounds of infiltration	Weight gain normalized by cell weight	
							For particle stability testing	For electrochemical testing
Ni	Ni	N/A	Nitrate decomposition	N/A	4M	1	1.34%	N/A
Ni-GDC	Ni - Gd _{0.1} Ce _{0.9} O _{2-δ}	1:1	Nitrate decomposition	N/A	4M	1	1.33%	1.24%
Ni-LSNC	Ni - La _{0.6} Sr _{0.3} Ni _{0.15} Cr _{0.85} O _{3-δ}	1.5:1	Citrate-nitrate auto-combustion	3:1	1M	5	1.88%	1.91%

2.2. Infiltration and microstructural characterization of button cells

Anode-supported SOFC button cells were purchased from SOFCMAN Energy (Ningbo, China). The cells were composed of a 400 μ m thick, 3 cm diameter NiO-YSZ anode bulk layer, a 5 μ m thick NiO-YSZ AAL, an 8 μ m thick dense YSZ electrolyte, a 15 μ m thick and 1.6 cm diameter strontium doped lanthanum manganite (LSM) YSZ composite cathode active layer, and a 30 μ m thick LSM cathode current collector layer. The electrochemically active area of the cell, determined by the cathode diameter, was 2 cm².

All cells were prepared for infiltration followed by electrochemical testing by pre-reducing the NiO-YSZ anode to Ni-YSZ. This process opens the pores of the anode, allowing the infiltrant to penetrate all the way through the anode and into the AAL. The procedures for anode pre-reduction and infiltration of the precursor solutions into the anode under vacuum have been detailed in a previous publication [14]. After infiltration of the precursor solution, both the Ni-GDC and Ni-LSNC cells were heated in air to 100°C and held for 20 minutes to evaporate the ethanol, then heated to 320°C and held for 20 minutes to react the metal nitrate precursors. For the Ni-GDC solution, heating to 320°C in air causes the decomposition of the Gd, Ce, and Ni nitrates into their respective oxides. For the Ni-LSNC solution, heating to 320°C in air causes the decomposition of the Ni nitrate into NiO, and also causes the citric acid and nitrates to combust, forming the LSNC phase.

For initial characterization of the microstructure of infiltrated cells, the infiltrated anodes were heated to 800°C while flowing a 2% H₂ – 98% Ar gas mixture at 300 cm³ min⁻¹ and held at temperature for 1 hour, allowing the Ni-GDC and Ni-LSNC to completely equilibrate to the anode operating environment before returning to room temperature. Cells processed in this way are later referred hereon as ‘as-reduced’. The surface morphology of the nanostructures of the Ni-GDC infiltrated, and Ni-LSNC infiltrated cells were examined using a field emission Zeiss (Carl Zeiss AG, Germany) SUPRA 55-VP scanning electron microscope (SEM) with an In-Lens secondary electron detector on fracture cross-sections of the samples. Higher spatial resolution images and elemental mapping of the Ni-GDC and Ni-LSNC nanostructures were also obtained on an FEI (ThermoFisher Scientific Inc., USA) Tecnai Osiris transmission electron microscope (TEM) equipped with an energy dispersive x-ray (EDX) detector. The TEM was operated at 200 keV in the scanning transmission electron microscopy (STEM) mode. Samples for STEM/EDX analysis were prepared by the conventional ‘lift-out’ technique in a FEI (ThermoFisher Scientific Inc., USA) Quanta 3D FEG focused ion beam (FIB) system.

2.3. Particle stability testing

Three pre-reduced cells were infiltrated with Ni, Ni-GDC, and Ni-LSNC respectively for particle stability testing. The weight gain of each cell after infiltration and heating to 320°C in air is reported in Table I. Each infiltrated cell was then fractured into three pieces. Each piece was first heated to 800°C under a 2% H₂ – 98% Ar gas mixture flowing at 300 cm³ min⁻¹ and then exposed to different atmospheric conditions at 800°C. One piece from each type of infiltrated cell was held under the same atmosphere (flowing 2% H₂ – 98% Ar gas mixture) for 1 hour, at which point all the NiO was reduced to Ni. These will be referred to hereon as ‘as-reduced’ samples. The second piece from each type of cell was held under the same atmosphere for a longer period of 48 hours. The third piece of each type of sample was exposed to a 25% H₂ – 75% H₂O gas mixture flowing at 300 cm³ min⁻¹ for 48 hours. Fracture cross-section SEM images of the AAL were recorded from each piece for analysis.

2.4. Electrochemical testing

Uninfiltrated, Ni-GDC infiltrated, and Ni-LSNC infiltrated cells were electrochemically tested to study the effect of Ni-MIEC infiltration on electrode performance. All cells were pre-reduced, and then the Ni-GDC and Ni-LSNC cells were infiltrated using their respective precursor solutions. The rounds of infiltration and weight gain after the heating procedure in air are shown in Table I. In preparation for electrochemical testing, a silver mesh (Alfa Aesar, USA) was then adhered to the cathode surface using silver ink (Alfa Aesar, USA) and dried in air at 80°C. Nickel ink (Fuel Cell Materials, USA) was then painted onto the anode surface and the cell was placed on top of the nickel mesh current collector (Alfa Aesar, USA) before assembling the electrochemical testing stand, which has been detailed in a prior publication [13]. The cell was placed between two Al₂O₃ tubes and the anode and cathode electrodes were gas sealed by using mica gaskets and glass paste. The entire assembly was spring-loaded between two aluminum end plates using Al₂O₃ rods for rigidity and to compress the mica gaskets. Nickel lead wires (Alfa Aesar, USA) on the anode side and silver lead wires (Alfa Aesar, USA) on the cathode side were protected by feeding them through small Al₂O₃ tubes. Al₂O₃ tubes were also used for inlet and outlet gas tubes on both anode and cathode sides. Cell

temperature was monitored during electrochemical testing using a K-type thermocouple placed in the cathode side chamber approximately 1 cm away from cell.

After assembly, the electrochemical testing stand was placed in a furnace and heated to 800°C, as measured by the cathode side thermocouple, at 1°C min⁻¹. During heating, 1 L min⁻¹ of dry air was flowed on the cathode side and 300 cm³ min⁻¹ of a 5% H₂ – 98% Ar gas mixture was flowed on the anode side. Once at temperature, the cell was held under open circuit condition for 12 hours to allow time for the glass paste to cure, and then the anode gas mixture was changed to 97% H₂ – 3% H₂O. The quality of the gas sealing was then evaluated by monitoring the cell's open circuit potential for the following 12 hours. The cell was then activated by applying 0.5 A cm⁻² of current for 48 hours. Cell performance was measured at temperatures of 800°C, 750°C, and 700°C. I-V scans and EIS were used to evaluate cell performance. I-V scans were recorded from OCV to 700 mV at a rate of 5 mA s⁻¹. EIS scans were recorded at open circuit conditions using an AC amplitude of 30 mV between 200000 Hz and 0.02 Hz. After performance measurement, cells were cooled to room temperature and prepared for microstructural characterization.

2.5. Microstructural characterization after electrochemical testing

Fracture cross-section SEM images of the AAL were recorded from the uninfiltated, Ni-GDC infiltated, and Ni-LSNC infiltated cells after electrochemical testing. Two distinct regions within the AAL: under the cathode, which is electrochemically active, and not under the cathode, which is not electrochemically active, were examined to evaluate the stability of the infiltated nanoparticles after exposure to both the testing environment and electrochemical current.

To measure the porosity of the uninfiltated, Ni-GDC infiltated, and Ni-LSNC infiltated cells after electrochemical testing, pieces of the fractured cells were infiltated with epoxy and allowed to cure at room temperature. Epoxied samples were then polished, and SEM images were taken at 50 micron intervals, starting at the anode/electrolyte interface, all the way across the 400 micron thick anode. At each depth, three images were taken at 40 kX magnification. The porosity was measured by segmenting out the pores

from each image using Avizo 3D (ThermoFisher Scientific Inc., USA), calculating the fraction of pore area from each image, and then calculating the average value of the three measurements. The pore occupation ratio, which is a simple measure of how much pore volume is occupied by the infiltrants, was then calculated using Equation 1.

$$\text{Pore Occupation Ratio} = \frac{\text{Porosity of Uninfiltrated Cell} - \text{Porosity of Infiltrated Cell}}{\text{Porosity of Uninfiltrated Cell}} = \frac{\text{Volume of Infiltrant}}{\text{Porosity of Uninfiltrated Cell}} \quad (1)$$

3. RESULTS AND DISCUSSION

3.1. Validation of MIEC Synthesis

Validation of Ni-GDC and Ni-LSNC as suitable materials for infiltration into Ni-YSZ cermet anodes requires that they meet the following four criteria: i) the Ni-MIEC precursors can be dissolved in a liquid solution; ii) the Ni-MIEC composite can be synthesized in the anode operating environment; iii) the infiltration solutions successfully penetrate through the entire anode and deposit nanoparticles within the AAL; and iv) the nickel nanoparticles are in contact with and stabilized by the MIEC. The first criterion is met by simply finding a solvent that can dissolve the precursors, ideally with a high concentration, and maintain a low enough viscosity to enable infiltration. Both GDC and LSNC nitrate precursors dissolve readily into ethanol at 70°C. Details of the precursor solutions are shown in Table I. The inclusion of citric acid makes the molarity of the Ni-LSNC metal ion precursors to be lower than that of the citric acid free Ni-GDC metal ion precursors, so more infiltration cycles are required for the Ni-LSNC infiltration.

The second criterion is validated by measuring the crystal phase using powder XRD after exposure to the reducing gas at 800°C. θ -2 θ x-ray diffraction scans of Ni-GDC and Ni-LSNC powders are shown in Fig. 1a and Fig. 1b respectively. The scans match the nickel plus fluorite and nickel plus perovskite target product patterns, respectively, confirming that the Ni-GDC and Ni-LSNC composites are properly formed from their respective precursor solutions. The third criterion is validated by infiltrating pre-reduced Ni-YSZ anodes with the Ni-MIEC precursor solution. Fig. 2b-c show SEM micrographs of the AAL of the Ni-GDC infiltrated and Ni-LSNC infiltrated cells after reduction at 800°C. Good area coverage and nanoparticle

connectivity is clearly observed in both cells, confirming that both Ni-MIEC infiltration solutions successfully penetrate through the anode.

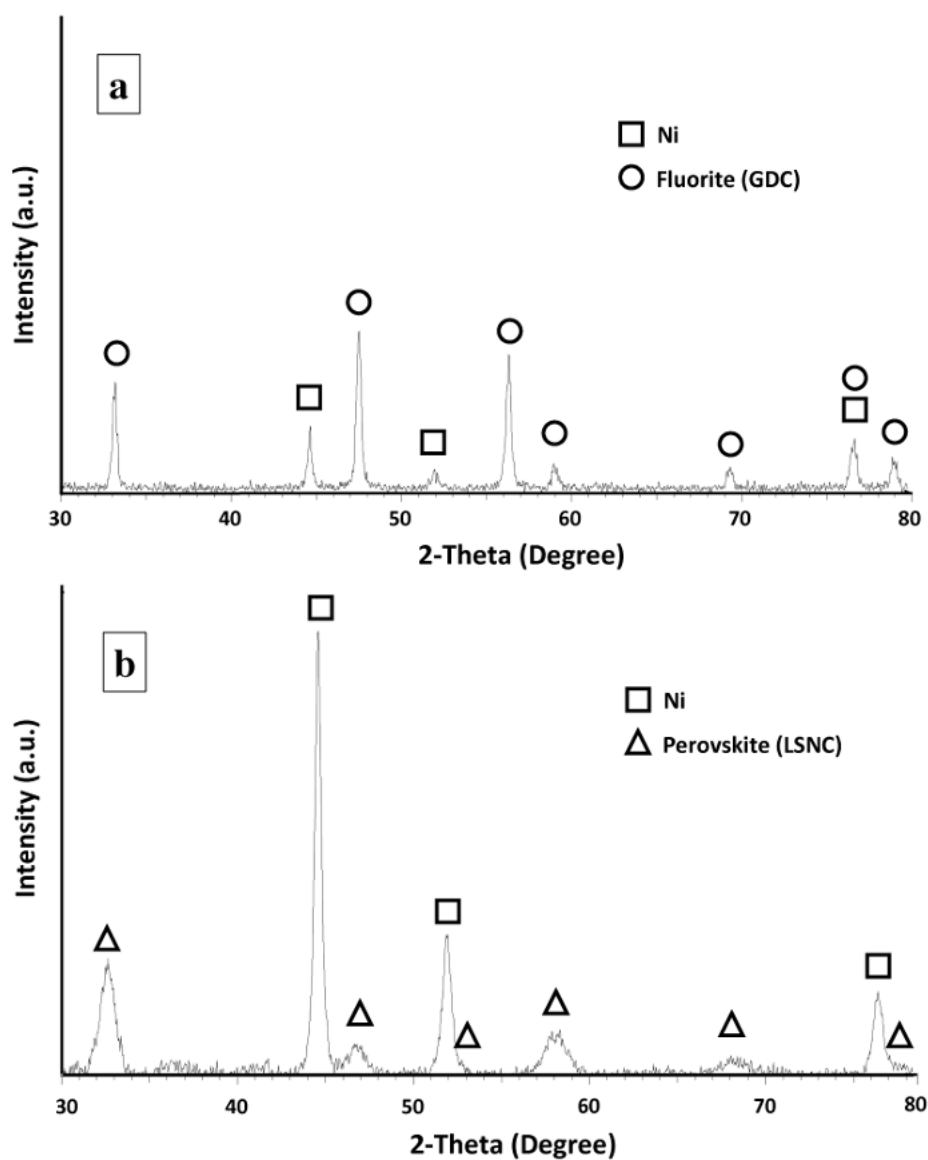


Fig. 1. θ - 2θ x-ray diffraction scans of a) Ni-GDC and b) Ni-LSCN powders synthesized from their respective precursor solutions. The scan shows that phase pure Ni-GDC and Ni-LSNC powder mixtures were successfully synthesized.

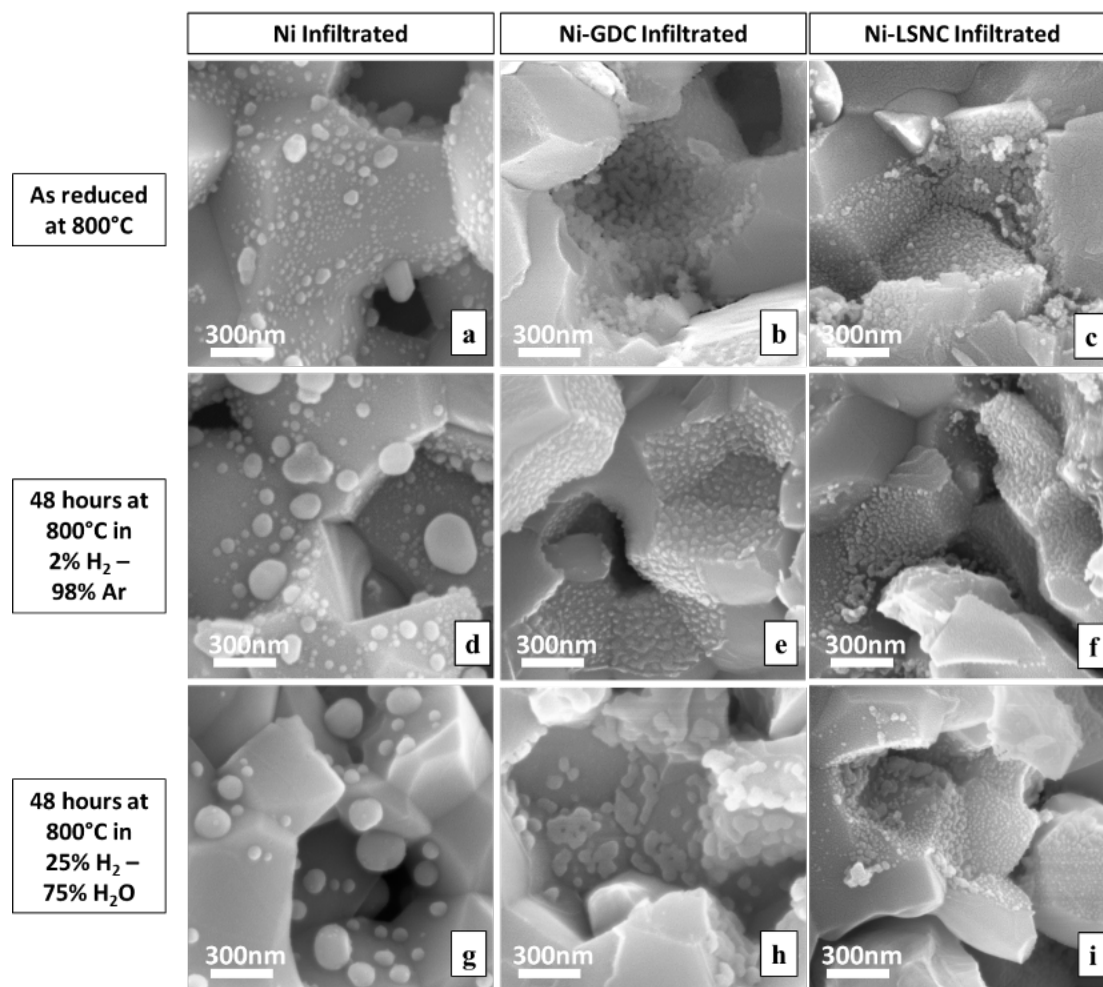


Fig. 2. Bright-field SEM micrographs of the AAL regions in fracture cross-sections of Ni infiltrated, Ni-GDC infiltrated, and Ni-LSNC infiltrated cells. a)-c) show the nanoparticles in the as reduced state; d)-f) show the nanoparticles after a 48 hour exposure in flowing 2% H₂ – 98% Ar gas mixture at 800°C; and g)-i) show the nanoparticles after a 48 hour exposure in flowing 25% H₂ – 75% H₂O gas mixture at 800°C.

In order to validate the fourth criterion, the individual nickel and MIEC particles need to be distinguishable. Cross-sectional high angle annular dark field (HAADF) STEM images of the pores and adjacent grains with elemental distributions in the AAL layer for the Ni-GDC and Ni-LSNC infiltrated cells after electrochemical testing are presented in Fig. 3. The nanoparticles in Ni-GDC and Ni-LSNC infiltrated cells are essentially connected with each other and also with cermet Ni grains. The results of the STEM/EDX elemental mapping shown in Fig. 3 also suggest that while Ni-GDC simply wets the surface of the Ni-YSZ grains, the Ni-LSNC fills a substantial amount of space within the pore. Also, in the Ni-GDC infiltrated cell, the rounded nickel nanoparticles are only deposited on YSZ grains, while in the Ni-LSNC infiltrated

cell, the nickel nanoparticles can be found in the vicinity of both YSZ and Ni grains. These differences are likely due to the citrate-nitrate combustion reaction needed to form the LSNC phase, which causes a rapid gas expansion during the heating procedure.

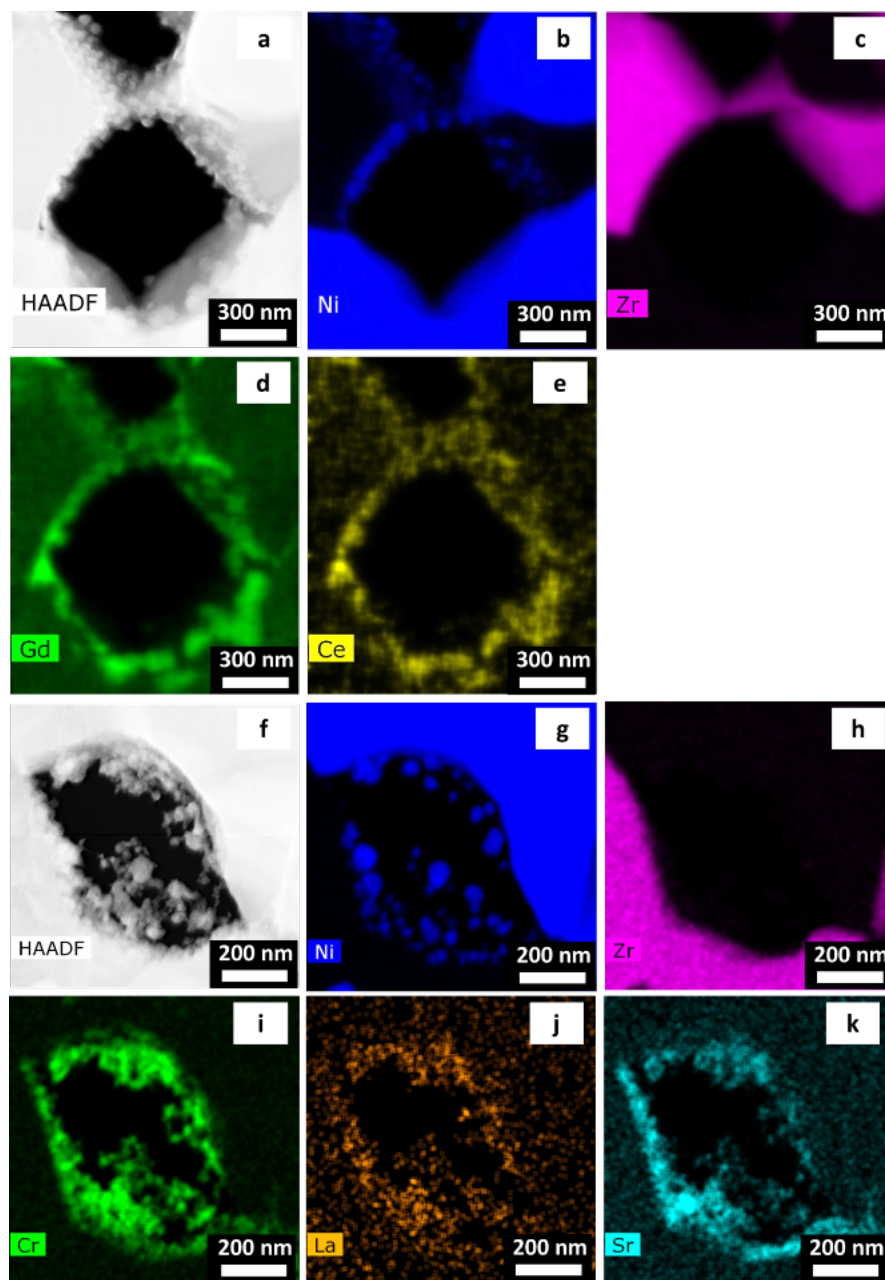


Fig. 3. a) HAADF STEM micrograph of the AAL of the Ni-GDC infiltrated cell after electrochemical testing, with elemental EDX maps of b) Ni, c) Zr, d) Gd, and e) Ce. f) HAADF STEM micrograph of the AAL of the Ni-LSNC infiltrated cell after electrochemical testing, with EDX dot maps of g) Ni, h) Zr, i) Cr, j) La, and k) Sr.

3.2. Stability of infiltrated nanoparticles

In order to qualitatively show the effects of MIEC infiltration on the stability of the nickel nanoparticles, the microstructures of nickel infiltrated, Ni-GDC infiltrated, and Ni-LSNC infiltrated anodes are compared after reduction at 800°C, after a 48 hour exposure to the reducing environment at 800°C, and after 48 hour exposure to a 25% H₂ – 75% H₂O at 800°C. The humid atmosphere accelerates the coarsening of nickel nanoparticles, due primarily to the increased wetting of nickel on YSZ surfaces, although the contact angle decreases sharply only when humidity levels go above 95% [11,14,29-31]. Investigation of the nickel infiltrated anode (Figs. 2a, 2d, 2g) reveals that infiltrated nickel nanoparticles with diameters less than 50 nm are unstable after the 48 hour exposure to high temperature in dry hydrogen (Fig. 2d). After the 48 hour exposure to a humid gas mixture (Fig. 2g), nearly all nanoparticles with diameters less than 100 nm disappeared. By comparison, nanoparticles in both the Ni-GDC infiltrated (Fig. 2b, 2e, 2h) and Ni-LSNC infiltrated (Fig. 2c, 2f, 2i) samples maintain stable and connected features of less than 100 nm, demonstrating that the additional oxide phases inhibit Ni nanoparticle coarsening. This is likely because the oxide phases pin the Ni nanoparticles, thereby blocking direct contact between them.

3.3. Electrochemical performance

The results of electrochemical testing of the uninfiltrated, Ni-GDC infiltrated, and Ni-LSNC infiltrated cells are shown in Fig. 4, and performance data from these measurements are listed in Table II. The I-V plots (Figs. 4a-4c) and the power density data (Table II) shows that the Ni-GDC infiltrated cell has the best performance and that the Ni-LSNC cell has a slightly higher performance compared to the uninfiltrated cell. The most obvious trend is that the performance of the Ni-GDC cell relative to the uninfiltrated cell increases as the operation temperature of the cell decreases; at 800°C, the Ni-GDC infiltrated cell has 30% greater power at 750 mV, while at 700°C it has 56% greater power at 750 mV. This implies that the infiltration of Ni-GDC into the anode improves charge transfer kinetics, because charge transfer resistance increases quickly when cell temperature is lowered, while the increase in mass transfer resistance is very small [32,33].

The Ni-GDC infiltration appears to have only a small impact on mass transfer resistance, because the cell performance is improved at 800°C, when cell performance is most sensitive to the kinetics of mass transfer. This is in contrast to the Ni-LSNC infiltrated cell, which shows a negligible performance increase at 800°C. The Ni-LSNC infiltrated cell does have some small improvement compared to the uninfiltrated cell as the operation temperature reduces, showing an 11% increase in power at 700°C. This suggests that Ni-LSNC does improve the charge transfer of the cell, but this is clearly at the cost of the increased mass transfer resistance.

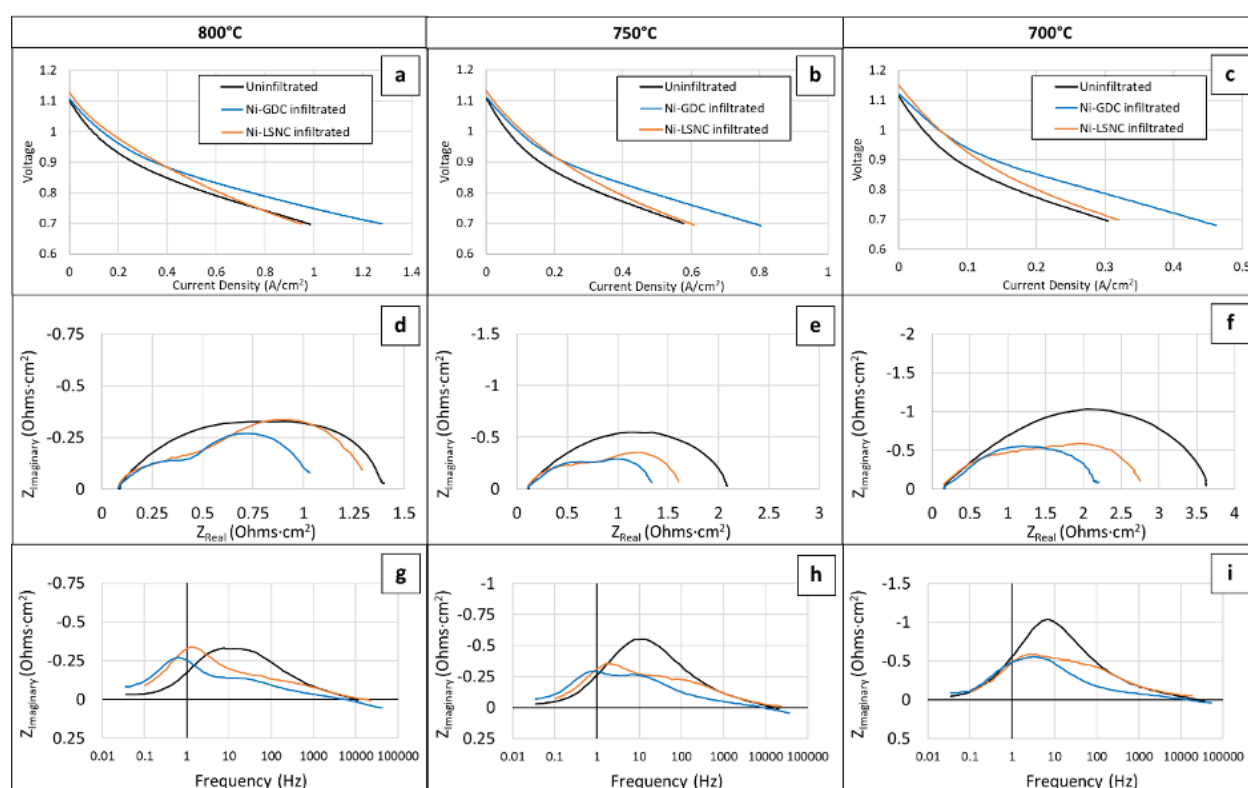


Fig. 4: Electrochemical performance measurements of uninfiltrated, Ni-GDC infiltrated, and Ni-LSNC infiltrated cells recorded at 800°C, 750°C, and 700°C with 3% humidified hydrogen flowing over the anode and dry air flowing over the cathode. Measurements include a)-c) I-V scans, and EIS measurements plotted in d)-f) Nyquist, and g)-i) and Bode formats.

Analysis of the EIS measurements supports these conclusions. The improvement of the polarization resistance for both Ni-GDC infiltration and Ni-LSNC infiltrated cell increases as the operation temperature decreases, as shown by the Nyquist plots in Figs. 4d-4f and in Table II. This trend corresponds to an

improvement of the anodic charge transfer kinetics after infiltration of the Ni-MIEC composites. However, Ni-LSNC shows less improvement than Ni-GDC. The Bode plots presented in Figs. 4g-4i reveal that at 800°C, the Ni-LSNC infiltrated cell has a noticeably large peak at about 1 Hz. This peak corresponds to the anodic mass transfer process, which is the slowest physical process of the cell. This demonstrates that the Ni-LSNC infiltrated cell suffers from poor mass transfer characteristics, limiting cell performance at higher temperatures. The Ni-GDC cell also has a peak around 1 Hz, but the peak height is much smaller than that for the Ni-LSNC cell. This indicates that the mass transfer resistance of the Ni-GDC infiltrated cell is has not been increased substantially compared to the uninfiltrated cell. As operation temperature is reduced, both anodic and cathodic charge transfer resistances increase and the mass transfer peaks becomes less distinct. However, Ni-LSNC still exhibits lower performance than Ni-GDC. From this result, it is clear that the Ni-GDC is a more effective infiltrant than the Ni-LSNC.

Table II. Performance data from EIS and I-V measurements of uninfiltrated, Ni-GDC infiltrated, and Ni-LSNC infiltrated cells.

R _{Polarization} ($\Omega \cdot \text{cm}^2$) (97% H ₂ – 3% H ₂ O anode, 21% O ₂ cathode)					
Temperature	Uninfiltrated	Ni-GDC infiltrated	Change	Ni-LSNC infiltrated	Change
800°C	1.31	0.95	-27%	1.20	-8%
750°C	1.97	1.23	-38%	1.49	-24%
700°C	3.47	2.05	-41%	2.60	-25%
R _{Ohmic} ($\Omega \cdot \text{cm}^2$) (97% H ₂ – 3% H ₂ O anode, 21% O ₂ cathode)					
Temperature	Uninfiltrated	Ni-GDC infiltrated	Change	Ni-LSNC infiltrated	Change
800°C	0.09	0.08	-10%	0.10	+6%
750°C	0.12	0.11	-8%	0.12	-1%
700°C	0.16	0.15	-5%	0.16	-2%
Power Density at 750 mV ($\text{W} \cdot \text{cm}^{-2}$) (97% H ₂ – 3% H ₂ O anode, 21% O ₂ cathode)					
Temperature	Uninfiltrated	Ni-GDC infiltrated	Change	Ni-LSNC infiltrated	Change
800°C	0.57	0.74	+30%	0.57	+0%
750°C	0.34	0.47	+39%	0.36	+6%
700°C	0.17	0.27	+56%	0.19	+11%

The decrease in polarization resistance for the Ni-MIEC (LSNC/GDC) infiltrated samples can be explained by the presence of additional activated TPBs and possible expansion of the region of charge transfer around the active TPBs. Both resulting in increased charge transfer reactions per unit area of the cathode and effective lowering of the polarization resistance. Depending on the spacing between the Ni nanoparticles and the Ni-YSZ backbone, the LSNC being primarily electronically conducting could provide an electronic pathway, thereby activating additional TPBs. Although GDC is not considered a good electronic conductor, its partial electronic conductivity is substantially higher than YSZ and its ionic conductivity comparable. In this case, the likely mechanism for improved performance is due to the expansion of the charge transfer region around the active TPBs associated with GDC. GDC is also reported to have a higher catalytic activity which could also be responsible for the improved performance.

3.4. Anode microstructures after electrochemical testing

In a previous study it was shown that infiltrated Ni nanoparticles coarsen during electrochemical testing, resulting in a reduction of the added TPB density, leading to a decrease in cell performance [13]. To analyze the impact of the cell testing procedure on the stability of the infiltrated features, two different fracture cross-section regions of the AAL of each cell after electrochemical testing were studied by SEM: the ‘electrochemically inactive region’ that is not under the cathode, and the ‘electrochemically active’ region which is under the cathode (Fig. 5a). The ‘electrochemically inactive’ region has been exposed to the testing environment, but does not experience any electrochemical current and anodic reactions due to the lack of a cathode above this region. The ‘electrochemically active’ region has been exposed to both the testing environment as well as the effects of electrochemical current and anodic reactions. SEM micrographs taken from the ‘electrochemically inactive’ regions are shown in Figs. 5b-5c, while those from ‘electrochemically active’ regions are shown in Figs. 5d-5e. Comparing these microstructures to the ‘as-reduced’ microstructures (Figs. 2b-2c) shows the effects of exposure to high temperature, reducing environment, and electrochemical current and reactions on the stability of the infiltrated Ni-GDC and Ni-LSNC nanostructures.

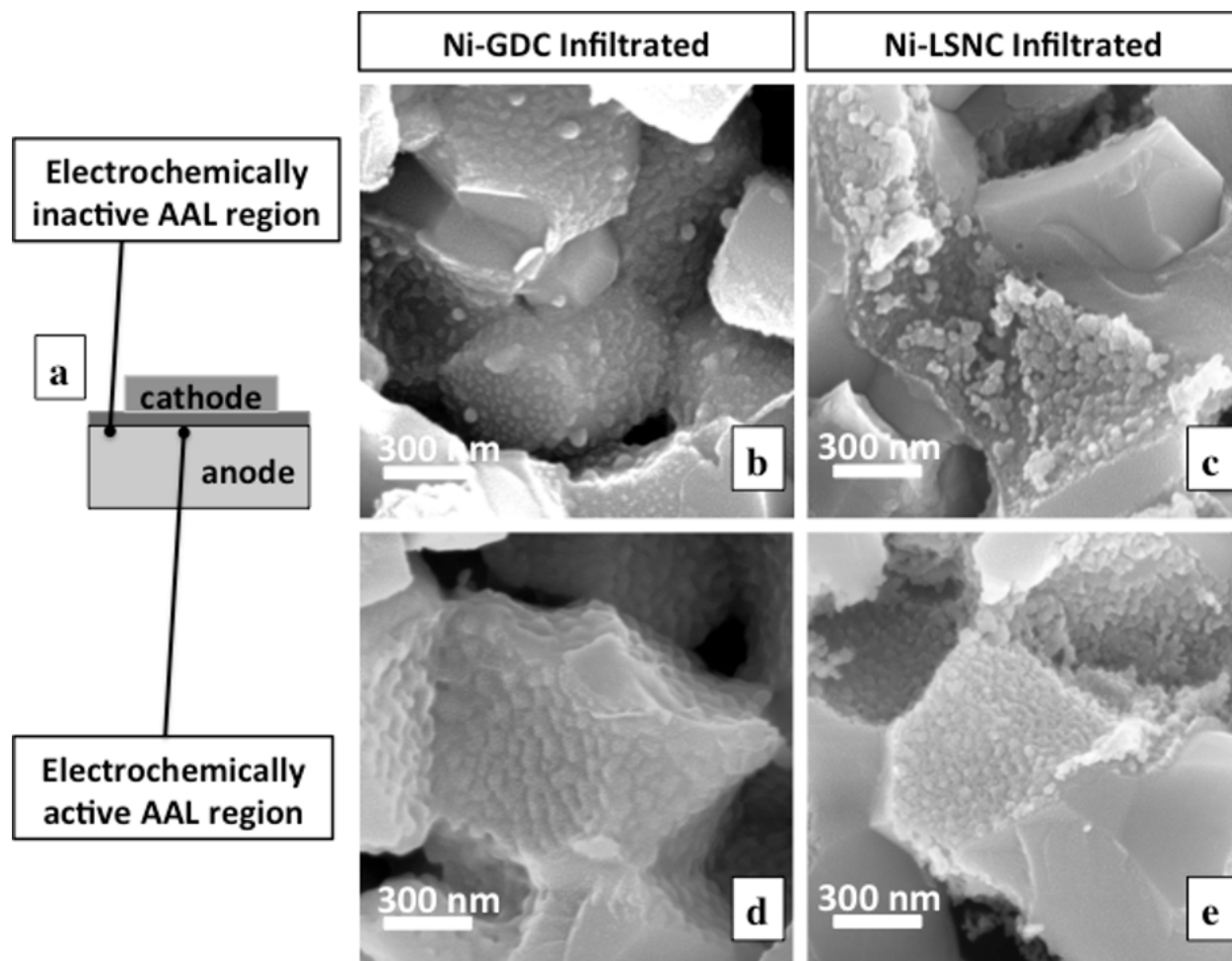


Fig. 5. a) Schematic of the cell showing the locations of ‘electrochemically inactive’ (not under cathode) and ‘electrochemically active’ (under cathode) regions in the AAL. Fracture cross-section SEM bright-field images of infiltrated Ni-GDC and Ni-LSNC nanoparticles in the b)-c) ‘electrochemically inactive’, and d)-e) ‘electrochemically active’ regions of the AAL.

Comparing Fig. 2c to Fig. 5c shows some evidence of increased agglomeration (since individual nanoparticles are still clearly visible, this is a case of agglomeration rather than coarsening) of Ni-LSNC nanoparticles after the additional 72 hours of exposure to the atmosphere at 800°C during the electrochemical testing (see Sec. 2.4 for details of electrochemical testing procedure) without exposure to the electrochemical current and chemical reactions. Comparing Fig. 2b to Fig. 5b shows significantly less agglomeration of the Ni-GDC nanoparticles after the additional high temperature exposure. Interestingly, Figs. 5d-5e show that exposure to electrochemical current and reactions cause both the Ni-GDC and Ni-LSNC nanostructures to spread evenly across the Ni-YSZ grains. This may actually be beneficial for the

stability of the electrode, because the infiltrated nanoparticles are now more homogeneously distributed, preventing the formation of hot spots with very high local current density that may lead to accelerated nanoparticle coarsening. Such ‘spreading’ due to lowering of the contact angle has been previously observed for infiltrated Ni nanoparticles during electrochemical testing [14], and similar principles are likely at play for the Ni-GDC and Ni-LSNC microstructures. Generally, both Ni-GDC and Ni-LSNC nanoparticles appear to be stable in the ‘electrochemically active’ AAL regions, which is where the majority of the anodic electrochemical reactions occurs. This stability reflects the advantages of the MIEC phase keeping the Ni nanoparticles isolated from one another and the stability of the nanoparticles is good for persistence of the long-term benefits of anode infiltration.

In order to better understand the increase of mass transfer resistance observed during electrochemical testing (Sec. 3.3), the porosity distribution throughout the anodes of different cells was obtained from the SEM images taken on polished cross-sections. The resulting porosity profiles for the uninfiltrated, Ni-GDC infiltrated, and Ni-LSNC infiltrated cells are shown in Fig. 6a. Each data point corresponds to the average porosity measured from three images with the uncertainty bars representing the maximum and minimum porosity. The uninfiltrated cell shows a nearly uniform porosity, while both the Ni-GDC and Ni-LSNC cells have a lower porosity throughout the entire anode. In general, the citrate-nitrate combustion process forms Ni-LSNC in a 3-D microstructure that occupies a larger volume fraction of the pores. The nitrate decomposition process forms Ni-GDC in a 2-D microstructure on the pores surface causing more modest pore filling. In particular, the Ni-LSNC cell shows dramatically reduced porosity near the anode-electrolyte interface. This could be expected because the individual pores of the AAL are smaller than the pores of the bulk anode.

The extent of pore filling can be seen clearly from the pore occupation ratio, which is calculated using Eq. 1 and shown in Fig. 6b. The pore occupation ratio is a measure of how much pore volume is filled by the infiltrants. When averaged across the whole electrode, the infiltration of Ni-GDC reduced the pore volume by 17.1% while the infiltration of Ni-LSNC reduced the pore volume by 28.6%. Assuming that the effective

diffusivity of the $H_2 - H_2O$ gas mixture varies linearly with the electrode porosity, this corresponds to a 17.1% and 28.6% reduction in the effective diffusivity of the Ni-GDC infiltrated and Ni-LSNC infiltrated cells, respectively. Assuming Fickian diffusion behavior in the anode, the mass transfer resistance of the electrode is inversely proportional to the effective diffusivity [34]. Thus, the filling of pores by infiltration results in a 20.6% increase in mass transfer resistance for the Ni-GDC infiltrated cell compared to the uninfiltrated cell, and a 40.1% increase in mass transfer for the Ni-LSNC infiltrated cell compared to the uninfiltrated cell.

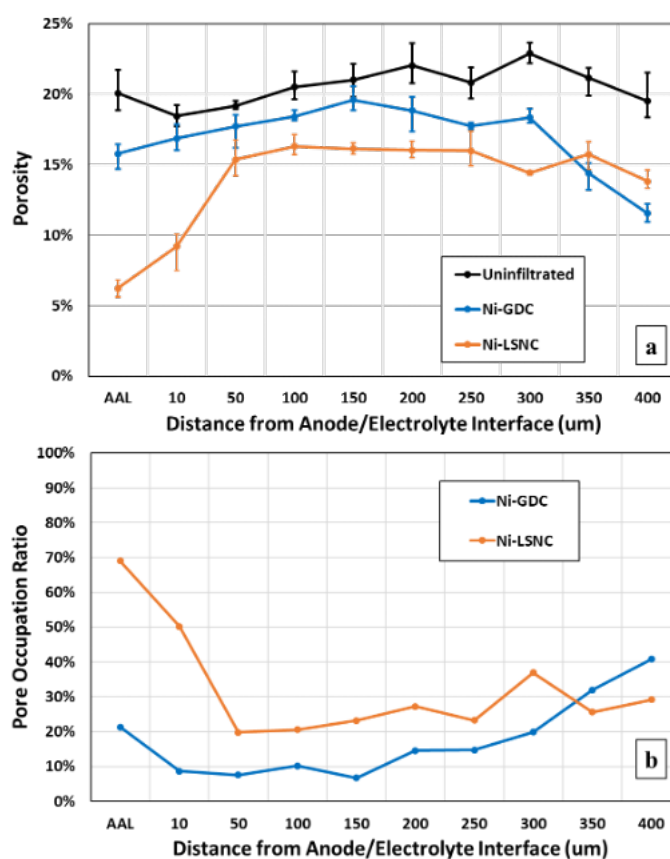


Fig. 6. a) Measured porosity profile across the anode cross-section of uninfiltrated, Ni-GDC infiltrated, and Ni-LSNC infiltrated cells. b) Calculated pore occupation ratio distribution across the anode cross-section for Ni-GDC infiltrated and Ni-LSNC infiltrated cells.

4. CONCLUSIONS

In this work, Ni-YSZ cermet anodes have been co-infiltrated with nanoparticles of Ni and a MIEC oxide phase. The roles of the conductive oxides were to provide a conductive pathway to electrically connect

some or all the Ni nanoparticles with each other and with the Ni-YSZ cermet anode, and to physically isolate them to avoid coarsening. Two oxides were chosen based on their chemical stability and conductivity in the anode operation environments: $\text{Gd}_{0.1}\text{Ce}_{0.9}\text{O}_{2-\delta}$, a predominantly ionic conductor, and $\text{La}_{0.6}\text{Sr}_{0.3}\text{Ni}_{0.15}\text{Cr}_{0.85}\text{O}_{3-\delta}$, a predominantly electronic conductor. Cells were successfully infiltrated to form Ni-GDC and Ni-LSNC nanostructures. The Ni-GDC and Ni-LSNC nanostructures were both more stable to 48 hour exposures to dry and 75% humid hydrogen atmospheres at 800°C, compared to only infiltrated Ni nanostructures.

The Ni-GDC infiltrated cell demonstrated substantially improved electrochemical performance at 800°C, 750°C, and 700°C, while the Ni-LSNC infiltrated cell only demonstrated a clear performance improvement at 700°C. Both Ni-GDC and Ni-LSNC infiltrated cells exhibited improved anodic charge transfer kinetics, but the Ni-LSNC cell also suffered from substantially increased mass transfer resistance. This was attributed to a 28.6% pore filling with a 3-D microstructure for the Ni-LSNC, as compared to a 17.1% pore filling with a 2-D microstructure for the Ni-GDC. The nanostructures in the ‘electrochemically active’ AAL regions of the cells remained resistant to significant coarsening and agglomeration, ensuring that the long-term benefits of the infiltration persist.

ACKNOWLEDGEMENTS

The research was funded in part by the Department of Energy, National Energy Technology Laboratory under award number DEFE0026096. The authors would also like to gratefully acknowledge the contributions of Dr. Zhihao Sun.

REFERENCES

- [1] J.T.S. Irvine, P. Connor, *Solid Oxide Fuel Cells: Facts and Figures / Past, Present and Future Perspectives for SOFC Technologies*, (Springer-Verlag, London, 2013). doi:10.1007/978-1-4471-4456-4.
- [2] R.P. O'Hayre, S.-W. Cha, W.G. Colella, F.B. Prinz, *Fuel Cell Fundamentals*, 1st ed., (John Wiley & Sons, Inc., Hoboken, New Jersey, 2016).
- [3] M. Boaro, A.S. Arico, eds., *Advances in Medium and High Temperature Solid Oxide Fuel Cell Technology*, (Springer Nature, Cham, Switzerland, 2017). doi:10.1007/978-3-319-46146-5.
- [4] E.D. Wachsman, K.T. Lee, *Science* 334 935–939 (2011). doi:10.1126/science.1204090.
- [5] J.M. Vohs, R.J. Gorte, *Adv. Mater.* 21 943–956 (2009). doi:10.1002/adma.200802428.
- [6] J.T.S. Irvine, D. Neagu, M.C. Verbraeken, C. Chatzichristodoulou, C. Graves, M.B. Mogensen, *Nat. Energy*. 1 15014 (2016). doi:10.1038/nenergy.2015.14.
- [7] J.H. Myung, D. Neagu, D.N. Miller, J.T. Irvine, *Nature*. 537 (2016). doi:10.1038/nature19090.
- [8] N. Mahato, A. Banerjee, A. Gupta, S. Omar, K. Balani, *Prog. Mater. Sci.* 72 141–337 (2015). doi:10.1016/j.pmatsci.2015.01.001.
- [9] X.M. Ge, S.H. Chan, Q.L. Liu, Q. Sun, *Adv. Energy Mater.* 2 1156–1181 (2012). doi:10.1002/aenm.201200342.
- [10] A. Bertei, J.G. Pharoah, D. a W. Gawel, C. Nicolella, *ECS Trans.* 57 2527–2536, 10 pp. (2013). doi:10.1149/05701.2527ecst.
- [11] L. Holzer, B. Münch, B. Iwanschitz, M. Cantoni, T. Hocker, T. Graule, *J. Power Sources*. 196 7076–7089 (2011). doi:10.1016/j.jpowsour.2010.08.006.
- [12] M. Kishimoto, Y. Kawakami, Y. Otani, H. Iwai, H. Yoshida, *Scr. Mater.* 140 5–8 (2017). doi:10.1016/j.scriptamat.2017.06.054.
- [13] Y. Lu, P. Gasper, U.B. Pal, S. Gopalan, S.N. Basu, *J. Power Sources*. 396 257–264 (2018). doi:10.1016/j.jpowsour.2018.06.027.
- [14] P. Gasper, Y. Lu, S.N. Basu, S. Gopalan, U.B. Pal, *J. Power Sources*. 410–411 (2019). doi:10.1016/j.jpowsour.2018.11.002.
- [15] A. Bertei, E. Ruiz-Trejo, K. Kareh, V. Yufit, X. Wang, F. Tariq, N.P. Brandon, *Nano Energy*. 38 526–536 (2017). doi:10.1016/j.nanoen.2017.06.028.
- [16] T. Klemensø, K. Thydén, M. Chen, H.J. Wang, *J. Power Sources*. 195 7295–7301 (2010). doi:10.1016/j.jpowsour.2010.05.047.
- [17] P. Keyvanfar, V. Birss, *J. Electrochem. Soc.* 161 F660–F667 (2014). doi:10.1149/2.056405jes.
- [18] E.F. Hardjo, D.S. Monder, K. Karan, *J. Electrochem. Soc.* 161 F83–F93 (2014). doi:10.1149/2.036401jes.

- [19] P.I. Cowin, C.T.G. Petit, R. Lan, J.T.S. Irvine, S. Tao, *Adv. Energy Mater.* 1 314–332 (2011). doi:10.1002/aenm.201100108.
- [20] T. Shimonosono, Y. Hirata, Y. Ehira, S. Sameshima, T. Horita, H. Yokokawa, *J. Ceram. Soc. Jpn.* 112 616–621 (2004). doi:10.14852/jcersjsuppl.112.0.S616.0.
- [21] S.P. Jiang, *Int. J. Hydrogen Energy*. 37 449–470 (2012). doi:10.1016/j.ijhydene.2011.09.067.
- [22] Z. Liu, B. Liu, D. Ding, M. Liu, F. Chen, C. Xia, *J. Power Sources*. 237 243–259 (2013). doi:10.1016/j.jpowsour.2013.03.025.
- [23] S.P. Jiang, Y.Y. Duan, J.G. Love, *J. Electrochem. Soc.* 149 A1175 (2002). doi:10.1149/1.1497982.
- [24] T.L. Skafte, J. Hjelm, P. Blennow, C. Graves, *J. Power Sources*. 378 685–690 (2018). doi:10.1016/j.jpowsour.2018.01.021.
- [25] E.C. Miller, Q. Sherman, Z. Gao, P.W. Voorhees, S.A. Barnett, *ECS Trans.* 68 1245–1254 (2015).
- [26] Y. Sun, J. Li, Y. Zeng, B.S. Amirkhiz, M. Wang, Y. Behnamian, J. Luo, *J. Mater. Chem. A*. 3 11048–11056 (2015). doi:10.1039/C5TA01733E.
- [27] R. Kiebach, P. Zielke, J.V.T. Hogh, K. Thyden, H.J. Wang, R. Barford, P. V. Hendriksen, *Fuel Cells*. 16 (2016). doi:10.1002/fuce.201500107.
- [28] R. Kiebach, C. Knöfel, F. Bozza, T. Klemensø, C. Chatzichristodoulou, *J. Power Sources*. 228 170–177 (2013). doi:10.1016/j.jpowsour.2012.11.070.
- [29] Z. Jiao, N. Shikazono, *Acta Mater.* 135 124–131 (2017). doi:10.1016/j.actamat.2017.05.051.
- [30] Z. Jiao, N. Shikazono, *J. Power Sources*. 396 119–123 (2018). doi:10.1016/j.jpowsour.2018.06.001.
- [31] A. Utz, H. Störmer, A. Leonide, A. Weber, E. Ivers-Tiffée, *J. Electrochem. Soc.* 157 B920 (2010). doi:10.1149/1.3383041.
- [32] V. Sonn, A. Leonide, E. Ivers-Tiffée, *J. Electrochem. Soc.* 155 B675 (2008). doi:10.1149/1.2908860.
- [33] A. Leonide, V. Sonn, A. Weber, E. Ivers-Tiffée, *J. Electrochem. Soc.* 155 B36–B41 (2008). doi:10.1149/1.2801372.
- [34] K.J. Yoon, P. Zink, S. Gopalan, U.B. Pal, *J. Power Sources*. 172 39–49 (2007). doi:10.1016/j.jpowsour.2007.03.003.